metals

Article

Degassing Window for Jet-Milled HPMS NdFeB Powder Recycled from Wind-Turbine Magnets: Hydrogen Desorption and Magnetic Recovery

Alba Berja [1,2,*], Laura Grau [3,4], Benjamin Podmiljsak [5], Spomenka Kobe [4,5], Carlo Burkhardt [3,4], Jose Francisco Fernández [1] and Adrián Quesada [1,*]

[1] Instituto de Cerámica y Vidrio (ICV), Consejo Superior de Investigaciones Científicas (CSIC), Calle Kelsen 5, 28049 Madrid, Spain; jfernandez@icv.csic.es
[2] Departamento de Física de Materiales, Facultad de Físicas, Universidad Complutense de Madrid, 28040 Madrid, Spain
[3] Institute for Precious and Technology Metals (STI), Pforzheim University, Tiefenbronner Str. 65, 75175 Pforzheim, Germany; laura.grau@hs-pforzheim.de (L.G.); carlo.burkhardt@hs-pforzheim.de (C.B.)
[4] Jožef Stefan International Postgraduate School, Jamova Cesta 39, 1000 Ljubljana, Slovenia; spomenka.kobe@ijs.si
[5] Department for Nanostructured Materials (K7), Jožef Stefan Institute, Jamova Cesta 39, 1000 Ljubljana, Slovenia; benjamin.podmiljsak@ijs.si
* Correspondence: alba.berja@csic.es (A.B.); a.quesada@icv.csic.es (A.Q.)

Abstract

Hydrogen processing of magnetic scrap (HPMS) is a promising short-loop route for recycling end-of-life NdFeB permanent magnets; however, the resulting hydrogenated powder requires vacuum degassing before reuse. This study defines a phenomenological degassing window for HPMS jet-milled powder from end-of-life wind-turbine magnets by screening degassing temperature (650–900 °C), heating rate (1–3 °C/min), and dwell time (5–60 min) under vacuum. Pressure–temperature desorption traces were deconvoluted into three Gaussian components ($R^2 = 0.999$), associated with hydrogen release from the $Nd_2Fe_{14}BH_x$ matrix and $NdH_{2.7}/NdH_2$ grain boundary phases, and correlated with SEM-EDS microstructural analysis and magnetic properties (H_c, M_r, and $M(1700\ kA\ m^{-1})$). Among the heating rates tested, 2 °C/min gave the most favorable combination of properties. Under this condition, the coercivity reached 434.1 kA/m after degassing at 900 °C, which we tentatively attribute to the recombination of α-Fe and Nd into $Nd_2Fe_{14}B$, while $M(1700\ kA\ m^{-1})$ peaked at 99.8 $A{\cdot}m^2/kg$ at 880 °C. Coercivity recovery depends primarily on the peak degassing temperature rather than on the time spent above 800 °C. The oxygen content increased from 0.46 wt.% after HPMS to 0.59 wt.% after jet milling and 0.66 ± 0.06 wt.% after degassing at 900 °C, which makes oxygen control a key limitation of the route. The results reveal a trade-off between coercivity and $M(1700\ kA\ m^{-1})$ that can be tuned within a single degassing step, and a degassing window distinct from that established for powders intended for re-sintering. The suitability of the recovered powder for bonded magnets remains to be demonstrated.

Keywords: short-loop magnet recycling; HPMS; degassing; permanent magnets; hydrogen desorption kinetics; NdFeB; end-of-life wind-turbine magnets

Check for updates

Academic Editors: Enrique Rocha-Rangel and Ivanovich Estrada-Guel

Received: 23 September 2026
Revised: 23 October 2026
Accepted: 27 October 2026
Published: 3 November 2026

Copyright: © 2026 by the authors. Licensee MDPI, Basel, Switzerland. This article is an open access article distributed under the terms and conditions of the Creative Commons Attribution (CC BY) license.

1. Introduction

Since their introduction to the market in 1984, neodymium-iron-boron (NdFeB) magnets have consistently held a leading position, attributed to their exceptional magnetic

properties, efficiency, and adaptability to diverse applications, e.g., home appliances, electronics, hybrid and electric vehicles, and wind turbines [1,2]. The rare-earth elements (REEs), such as Nd and Dy, present in NdFeB magnets are classified as critical raw materials (CRMs) for the green and digital transitions due to their substantially growing demand, high import dependency, and supply risks. The growing demand for CRMs related to economic growth and coupled with the need to build robust and sustainable supply chains underscores the importance of developing recycling methods. By implementing CRM recycling, a circular, cost-effective economy can be established while conserving Earth's natural resources and securing technological advancement.

Over the past few years, multiple recycling processes have been developed [3,4], encountering numerous challenges related to policy and regulation, economic, supply chains, and technological limitations [5]. These methods can be categorized into indirect or "long-loop" recycling, which relies on pyrometallurgical [6–8] or hydrometallurgical [9–11] treatments to extract individual REEs, which tend to be energy-intensive and generate significant chemical waste. In contrast, direct methods, also referred to as "short-loop" or "magnet-to-magnet" recycling, involve the recovery and utilization of the magnetic material for the fabrication of new permanent magnets, offering a more economical and environmentally friendly alternative route [6,12,13]. In addition to a 45% reduction in energy consumption, a 53% decrease in costs, and a saving of 11 tons of CO_2 per ton of magnet produced, these routes also mitigate supply chain risks within the EU [14]. The challenge in this case lies in the usually inferior properties of the recycled material.

Among these direct recycling processes, hydrogen processing of magnetic scrap (HPMS) is currently one of the most promising industrial approaches. Developed by researchers at the University of Birmingham [15], HPMS is based on hydrogen decrepitation, in which end-of-life magnets are exposed to hydrogen gas at room temperature and controlled pressures, leading to embrittlement and disintegration into a demagnetized, hydrogenated powder. This powder contains coarse $Nd_2Fe_{14}BH_x$ grains (~10 µm) and finer Nd-rich grain boundary phase (GBP) particles (~1 µm) [16]. To refine it into single-crystal (single-grain) particles suitable for magnet fabrication, the hydrogenated powder is typically further processed via jet milling in a protective atmosphere. This method accelerates particles through a high-pressure gas stream, promoting collisions that yield a fine powder (~5 µm) while minimizing oxygen uptake compared to other milling methods [17,18].

Despite the efficiency exhibited by the HPMS method, notable technological limitations exist, including the complexity of the process and the multitude of parameters impacting the recovery rate of magnetic properties in the final magnet. From a microstructural perspective, coercivity in sintered NdFeB magnets is controlled by the nucleation of reversed domains at grain surfaces and their propagation between grains, which is hindered by Nd-rich intergranular phases (typically α-Nd or Nd oxides) acting as non-magnetic barriers. These phases decouple the ferromagnetic $Nd_2Fe_{14}B$ grains, suppressing exchange interactions and hindering magnetization reversal [19–21]. Oxidation and contaminants found in the magnets, such as residues of coatings and glues, degrade the quality of the final magnet. Increased oxygen content leads to oxidation of the reactive Nd-rich grain boundary phase (GBP), forming Nd_2O_3, which reduces magnetic isolation of $Nd_2Fe_{14}B$ grains and decreases the amount of Nd in the GBP, limiting the liquid phase during sintering [22]. Since Nd_2O_3 has a higher melting point than Nd, exceeding the sintering temperature of NdFeB magnets, a protective atmosphere is necessary during recycling to prevent oxidation and consequently reduce coercivity loss [23]. Furthermore, the hydrogen present in the hydride phase must be removed via a degassing treatment (thermal desorption under vacuum) to restore magnetic properties prior to sintering or bonding processes. Residual hydrogen degrades the magnetic performance of the powder, in particular its coercivity. When hydrogen is

absorbed, it reacts with the Nd-rich grain boundary phases to form Nd hydrides, reducing their ability to decouple the matrix grains and causing a volume expansion of the GBP, resulting in stress and intergranular cracks [24,25]. Additionally, hydrogen can diffuse into the main matrix phase, resulting in transgranular fracture. The absorbed H_2 produces the reduction of the anisotropy field and subsequently the coercivity [26]. On the contrary, the hydride formation of the $Nd_2Fe_{14}BH_x$ phase increases M_s due to the increased volume of the unit cell [27]. Degassing also plays a crucial role in facilitating the magnetic alignment of NdFeB powders during magnet fabrication. As Wiesinger et al. [27] reported, hydrogen absorption alters the crystal field around Nd atoms, thereby reducing magnetocrystalline anisotropy and hindering particle alignment under an external magnetic field. Similarly, Fruchart et al. [28] demonstrated that hydrogen incorporation significantly modifies the magnetic parameters of the material, such as the Curie temperature, overall magnetization, and especially the anisotropy constants. This occurs through subtle changes in the crystalline electric field and exchange interactions within the rare-earth sublattice. Consequently, in the case of bonded magnet fabrication, the degassing (or dehydrogenation) step serves a dual purpose: it enhances alignment during compaction and improves the magnetic performance of the final magnet.

Several studies have investigated the possibility of recycling sintered NdFeB magnets following hydrogen desorption treatments, demonstrating that appropriate thermal protocols can significantly recover both coercivity and remanence. Table 1 summarizes the state-of-the-art. For instance, Zakotnik et al. [29] achieved a coercivity value of approximately 750 kA/m and a remanence of ~1.35 T after vacuum degassing hydrogen-decrepitated (HD) powders at 700 °C. Similarly, Sheridan et al. [30] optimized the hydrogenation–disproportionation–desorption–recombination (HDDR) process by reducing hydrogen pressure at 880 °C following the disproportionation stage in order to produce hydrogen desorption, and reported values of 0.94 T and 740 kA/m. Li et al. [31] demonstrated that vacuum degassing of recycled NdFeB powders to produce bonded magnets at 1073 K for 1 h restores the properties of the powder, enabling the fabrication of bonded magnets with magnetic properties of B_r = 0.9 T, H_{ci} = 841.4 kA/m, and $(BH)_{max}$ = 111.6 kJ/m^3. The optimization of the degassing process has been more scarcely explored in recycled powders produced via hydrogen processing of magnetic scrap (HPMS). HPMS is typically conducted at lower temperatures (25–400 °C) without a specific desorption step [32–34], whereas HDDR involves explicit desorption and recombination stages at elevated temperatures (600–950 °C) [1,35,36]. Given that the solubility and stability of hydride phases decrease with increasing temperature, hydrogen absorption is thermodynamically favored at lower temperatures and decreases at higher ones. As a result, HDDR-processed powders typically retain significantly less hydrogen than those processed via HPMS, where hydrogen can remain trapped within the microstructure due to the absence of a high-temperature degassing step. Once the magnetic properties are recovered, the resulting powder can be used as feedstock for the production of bonded NdFeB magnets [36–40].

Using HPMS jet-milled powder in polymer-bonded magnets faces several practical bottlenecks. First, unlike the sintering route, no later high-temperature step is available to complete hydrogen removal or restore the microstructure, so the degassing treatment alone must deliver the final magnetic properties of the powder. Second, the large specific surface area of jet-milled powder favors oxygen pick-up during handling, degassing, and compounding, consuming the Nd-rich phase on which coercivity depends [22]. Third, milling-induced surface defects and loss of a continuous grain boundary phase lower the coercivity of fine particles [21]. Fourth, particle size distribution and morphology govern powder flow, feedstock rheology, and mold filling, while the polymer binder dilutes the magnetic phase, so the properties of the loose powder set an upper bound for those of

the bonded component [39]. Moreover, most commercial bonded magnets use melt-spun isotropic powders with nanocrystalline microstructures or anisotropic HDDR powders with sub-micrometer grains [35,39]. Recycled HPMS powders, made of micrometer-sized single-crystal particles, rely on a different coercivity mechanism and must be benchmarked against these materials. Recovering the magnetic properties of the loose powder is, therefore, a necessary, but not sufficient, condition for its use in bonded magnets.

Despite this extensive body of work on hydrogen-assisted recycling of NdFeB magnets, a systematic study of vacuum degassing parameters on HPMS jet-milled powders, from EoL wind turbine magnets, combined with desorption kinetics and magnetic behavior correlation is, to the best of our knowledge, absent from the literature. The fundamental study of Zakotnik et al. on hydrogen-decrepitated powder from hard-disk voice-coil magnets [41] varied the degassing temperature between 200 and 1000 °C at a single fixed heating rate of 5 °C/min, with no controlled dwell. Their research identified an optimal temperature of 700 °C and established the thermal protocol that has since dominated the field. Subsequent studies have inherited those conditions, or close variants thereof, without revisiting the underlying parameter space. Li et al. [37] conducted a temperature sweep on sieved, non-jet-milled HD powder but only tracked the residual hydrogen content. Önal et al. [42] compared partial (PD) and full degassing (FD) in fixed binary categories as an input for an oxidation study. Mishra et al. [34] used a single degassing profile to qualitatively identify hydride phases. Rathfelder et al. [43] adopted a 600 °C/2 h protocol drawn from earlier literature [44] to support a powder-extrusion-molding workflow without further optimization. The most recent published study on HPMS jet-milled feedstock, by Kozak et al. [45], explicitly avoided degassing prior to re-sintering, identifying degassing optimization as a target for future work. Across this body of work, heating rate has not been treated as a design variable, dwell time has not been systematically varied, and no study has linked a quantitative analysis of the desorption trace to the magnetic and microstructural recovery of jet-milled material.

In this work, we present a systematic investigation of the effect of degassing temperature, together with a screening of heating rate, on the hydrogen desorption behavior and magnetic properties of jet-milled HPMS powder recycled from end-of-life (EoL) wind-turbine magnets (Figure 1 schematizes the process involved). The specific parameters investigated are temperature (650–900 °C), heating rate (1–3 °C/min), and dwell time (5–60 min). The pressure–temperature desorption trace is deconvoluted into three Gaussian components, attributed on the basis of previous studies to the hydride decomposition reactions ($Nd_2Fe_{14}BH_x \rightarrow Nd_2Fe_{14}B + (x/2)H_2$; $NdH_{2.7} \rightarrow NdH_2 + 0.35H_2$; $NdH_2 \rightarrow Nd + H_2$), and is correlated with quantitative microstructural analysis (SEM-EDS, particle and grain size distributions, oxide layer thickness, and grain boundary phase composition), oxygen analysis, and magnetic characterization (coercivity, remanence, $M(1700\ \text{kA m}^{-1})$) at each parameter combination.

By addressing the influence of heating rate as a processing variable and by relating the hydrogen desorption traces to the observed magnetic-property evolution, this work provides insight into the selection of degassing conditions for this specific recycled feedstock and establishes a basis for further process optimization. The study is designed as a processing-window screen on a single industrially processed batch of EoL feedstock. Its aim is to identify the degassing conditions that recover the magnetic properties of this powder, using the desorption traces to bound that window. The potential use of the recovered powder in bonded-magnet manufacturing remains a prospective application requiring subsequent validation through feedstock optimization and consolidation into bonded magnets in future research.

Table 1. Coverage of degassing parameters in prior hydrogen-based recycling studies of NdFeB compared with the present work. No prior study reports a combined sweep of degassing temperature, heating rate, and dwell on HPMS jet-milled powder. Feedstock, processing route, and target application differ between studies, so the table is intended to position the present work rather than to compare numerical results directly.

Reference	Feedstock	Target Application	Milling	Degassing T	Heating Rate	Dwell	Responses Tracked	Desorption Analysis—Magnetic Recovery Correlation
Williams and McGuiness, 1991 (J. Less-Common Met.) [44]	Sintered NdFeB-type alloys	Fundamental H_2 desorption study	None (bulk)	Single ramp to ~800 °C	Fixed (mass-spec ramp)	Not varied	H_2 desorption peaks	No (phase ID only)
Zakotnik, Harris and Williams, 2008 (JAC) [41]	HDD voice-coil sintered magnets	Re-sintered magnets	HD + roller ball mill	200–1000 °C (swept)	Fixed at 5 °C/min	"Until vacuum recovered" (not varied)	H_{cj}, B_r vs. T; particle size; SEM	Partial: peaks identified, no kinetic analysis
Sheridan et al., 2014 (JMMM) [30]	Sintered scrap (HDDR route)	Anisotropic HDDR powder	HD + HDDR (not jet-milled)	880 °C (single, within HDDR)	Not a design variable	Not varied	H_{cj}, B_r after HDDR	No (desorption embedded in HDDR)
Li et al. 2015 (JMCWM) [37]	Scrap sintered magnets	Anisotropic bonded magnets	HD + sieving (no jet mill)	550, 600, 650, 700 °C	Not specified/not varied	Not specified/not varied	Residual H content; bonded-magnet H_{cj}, B_r	No (no desorption-trace analysis)
Önal et al. 2017 (JAC) [42]	Sintered VCM + low/high-grade scrap	Assessment of recycling routes (oxidation)	HD + light grinding	300, 500 (PD), and 900 °C (FD)—binary categories	Fixed at 10 °C/min (in air, for DSC-TGA)	PD: 2 h; FD: 1 h—fixed	Oxidation (TGA), microstructure	No (focus is oxidation behavior, not magnetics)
Mishra et al. 2023 (Materials) [34]	Sintered NdFeB (J. Stefan Institute)	Matrix-phase recovery for short-loop recycling	HD only (no jet mill)	RT → 700 °C (single profile)	2 °C/min (single value)	Not varied	Pressure–T profile for hydride phase ID; ICP-MS; SEM; VSM	Qualitative phase identification
Rathfelder et al. 2025 (Sci. Rep.) [43]	EoL magnets via HPMS	Anisotropic magnets by powder extrusion molding	HPMS + vibratory milling	600 °C (fixed, adapted from 1991 protocol)	Not optimized	2 h (fixed)	PEM sintered magnet C, O, B_r, H_{cj}	No (degassing is a fixed pre-step)
Kozak et al. 2025 (SMT) [45]	HDD + production scrap via HPMS	Re-sintered magnets	HPMS + jet mill (cyclone classifier)	Not degassed prior to re-sintering	n/a	n/a	Re-sintered magnet B_r, H_{cj}; O, N content	Explicitly identifies degassing optimization as future work
This work *	**EoL wind-turbine magnets**	**Recovered powder; bonded magnets (prospective)**	**HPMS + jet mill (N_2)**	**650–900 °C (fine resolution 840–900 °C)**	**1, 2, 3 °C/min (swept)**	**5–60 min (swept)**	**H_c, M_r, M(1700 kA m^{-1}); SEM-EDS; particle/grain size; O content; deconvoluted P–T trace**	**Three-Gaussian deconvolution (R^2 = 0.999) coupled to magnetic and microstructural recovery**

* Note: The row highlighted in bold indicates the parameters investigated in the present study.

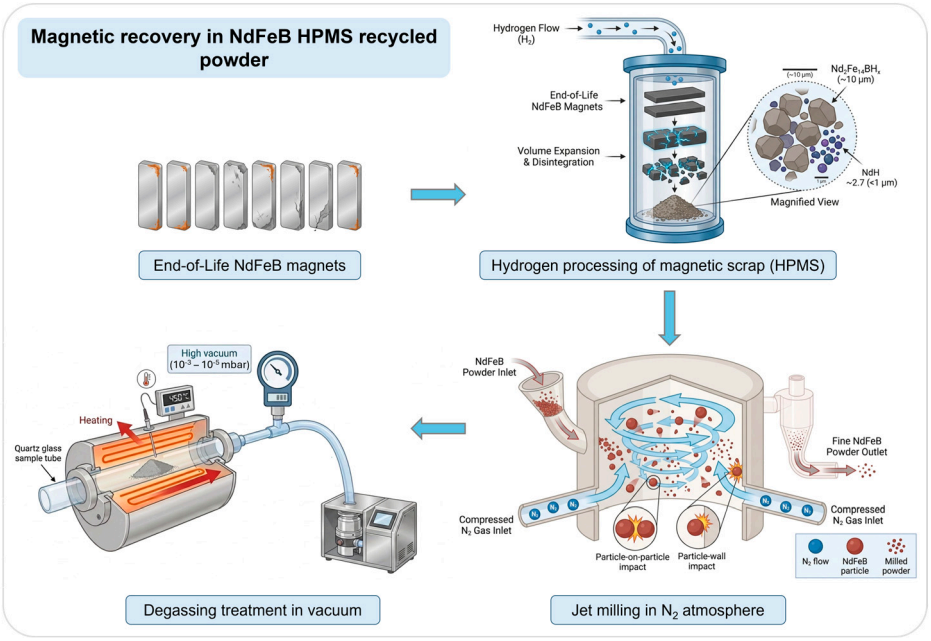


Figure 1. Illustration of the method developed for the recycling of magnets from EoL wind turbines, and the HPMS route used to produce the recycled powders studied here, with their prospective use in bonded magnets. Large blue arrows indicate the sequence of processing steps, while the smaller arrows illustrate process-specific details.

2. Materials and Methods

2.1. Starting Material and Recycling Process

EoL NdFeB magnets were collected from wind turbines by the Slovenian company Surovina d.o.o. The demagnetization curve of the extracted magnets was determined using a permeameter (Magnet-Physik Dr. Steingroever, Cologne, Germany). Also, the first microstructural characterization was studied in these EoL magnets using scanning electron microscopy (SEM) with a "Hitachi FlexSEM 1000 II" (Hitachi High-Tech, Tokyo, Japan). Subsequently, the EoL magnets underwent recycling via hydrogen processing [16], yielding a hydrogen-decrepitated powder that was subsequently jet-milled under N_2 atmosphere. All experiments in this work used powder from a single industrial-scale HPMS batch, so that differences between degassing conditions could not arise from batch-to-batch variations in feedstock composition, oxygen content, or microstructure.

2.2. Degassing Protocol, Desorption-Trace Analysis, and Kinetics Extraction

The fine powder was then thermally degassed at different temperatures in the range from 650 °C to 900 °C for 5–60 min under vacuum. The experimental program was conducted in two stages. An initial set of experiments was used to explore the influence of the heating rate on the magnetic properties of the recycled powder. Based on these results, a heating rate of 2 °C/min was selected for a subsequent set of experiments designed to investigate the effect of degassing temperature under otherwise comparable heating conditions. After the specified dwell time at the target temperature, the furnace was allowed to cool naturally to room temperature with the samples remaining inside. The cooling rate was not monitored. The pressure–temperature (P–T) evolution in the dehydrogenation process was studied by monitoring the heating of the samples at various temperatures and heating rates using a tube furnace (Nabertherm GmbH, Lilienthal, Germany) connected to a vacuum pump (Pfeiffer vacuum GmbH, Aßlar, Germany) under an initial vacuum of 10^{-3}–10^{-5} mbar. The pressure–temperature traces were smoothed and fitted to a sum of

three Gaussian components plus a constant baseline using a Levenberg–Marquardt algorithm. The goodness of fit was evaluated using the coefficient of determination (R^2), with values of 0.999 indicating an excellent agreement between the experimental profiles and the fitted curves. This approach was used as a phenomenological method to compare the positions and relative contributions of the individual components, rather than to establish a specific kinetic model. Under dynamic pumping at constant effective pumping speed, the pressure rise above the baseline is proportional to the instantaneous hydrogen desorption rate, so the P–T trace was treated as a thermal desorption spectrum [46]. Gaussian line shapes were used as an empirical description of peaks broadened by the particle size distribution, by the distribution of local hydrogen environments, and by the finite response of the furnace–pumping system. Individual first-order desorption peaks are intrinsically asymmetric, but the peak-maximum temperatures used in the kinetic analysis depend only weakly on the line shape. The assignment of the three components to specific hydride reactions is based on previous studies [44] and was not verified by in situ phase analysis in this work. Activation energies for the deconvoluted peaks were estimated using the Redhead approximation [46] under the assumption of first-order desorption kinetics and pre-exponential factors ν of 10^{11} and 10^{13} s^{-1}. Because ν cannot be determined from a single heating rate, these two values bracket the range typical of hydrogen desorption from metal hydrides—changing ν by two orders of magnitude changes E_a by about 13%. Furthermore, the limited number of heating rates does not allow a robust determination of activation energies using multi-ramp methods, such as the Kissinger approach. In this study, the heating rate dependence was primarily investigated in relation to hydrogen desorption behavior and magnetic-property recovery, whereas the activation-energy estimates provide an approximate comparison of the relative kinetic barriers associated with the different desorption processes. Accordingly, the interpretation focuses primarily on the relative ordering of the estimated activation energies rather than on their absolute values.

Each degassing condition was run at least twice. Additional runs were performed when the characteristic desorption peaks were absent or poorly resolved, particularly when this behavior was accompanied by severely degraded magnetic properties. These observations were considered potential indicators of unintended oxygen exposure during sample handling or thermal treatment in the tubular furnace. Repeated experiments were used to assess the reproducibility of the desorption profiles and to investigate whether the anomalous behavior occurred again. Since oxygen uptake was not directly established as the cause in every such case, this interpretation is considered tentative.

Because the samples were heated from room temperature, the time spent at high temperature is dominated by the heating ramp rather than by the dwell. To compare conditions with different heating rates and dwell times, the time spent at or above a threshold temperature T_{th} was calculated for each condition as $t_{th} = (T_{max} - T_{th})/\beta + t_{dwell}$ for $T_{max} \geq T_{th}$, where T_{max} is the degassing temperature and t_{dwell} the dwell time. The contribution of the uncontrolled furnace cooling was neglected. A threshold of 800 °C (t_{800}) was used because recombination of Fe with NdH_2 is reported to occur in the 800–900 °C range [30], and thresholds of 750 and 850 °C were used to test the sensitivity of the analysis.

2.3. Compositional Analysis

The composition of the HPMS and jet-milled HPMS powders was determined by inductively coupled plasma optical emission spectrometry (ICP-OES). Samples were digested in aqua regia (HCl:HNO_3 = 3:1 v/v) in closed vessels in a MARS 6 microwave digestion system (CEM Corporation, Matthews, NC, USA) at 200 °C. The digests were diluted to volume with 5 vol.% HNO_3, which was also the matrix of the calibration standards, and analyzed with an iCAP 7400 ICP-OES (Thermo Fisher Scientific, Waltham, MA, USA). Light

elements (O, N, H, C) cannot be determined by ICP-OES. Oxygen was measured separately, as described below.

The oxygen content was determined using a LECO ONH836 elemental analyzer (LECO Corporation, St. Joseph, MI, USA) by hot gas extraction followed by infrared detection of CO, with calibration against certified reference materials. It was measured on the HPMS powder, the HPMS jet-milled powder, and three specimens degassed at 900 °C with $\beta = 2$ °C/min—not enough material remained to analyze the other degassed samples.

2.4. Microstructural Characterization

To investigate the morphology of the samples using scanning electron microscopy (SEM), specifically the particle cross-section, the degassed powders were embedded in resin inside a glovebox, ground with SiC papers down to 10 µm, and polished with diamond polishing paste (9, 3, and 1 µm) to obtain a flat surface for electron microscopy. Microstructural characterization before and after degassings was performed using a field-emission-gun scanning electron microscope (FEGSEM) Verios G4 HP (Thermo Fisher Scientific Company, Hillsboro, OR, USA) equipped with an Aztec Live energy-dispersive X-ray spectroscopy (EDS) system (version 6.1, Oxford Instruments, Abingdon, UK) to confirm the elements present in the samples. The particle size distribution was obtained from the SEM images using ImageJ software (Version 1.51j8) [47], by counting approximately 350 particles. Additionally, the grain size was determined by measuring over 150 grains. Both parameters were calculated using the arithmetic mean of the statistical distribution of equivalent diameters, i.e., the diameter of a cross-sectioned circle with the same area as the grain.

2.5. Magnetic Characterization

The magnetic hysteresis curves of the samples were collected with a vibrating sample magnetometer (VSM "8600 series" Lake Shore Cryotronics, Inc., Westerville, OH, USA) at room temperature ($T = 298$ K) under an applied magnetic field up to ~1700 kA m^{-1} (~ 2 T). Note that the samples are not fully saturated, and magnetization at the maximum applied field is denoted as M(1700 kA m^{-1}). For the same reason, the coercivity H_c and remanence M_r obtained from these loops are operational values and represent lower limits of those that would be measured after full saturation. The powder was loaded in its loose state into disposable plastic powder sample cups (Lake Shore Cryotronics) inside a glovebox. The threaded cap was then tightened, compressing the powder inside the holder and limiting its exposure to atmospheric oxygen and moisture. The samples were measured immediately after removal from the glovebox to minimize potential oxidation during handling and transfer.

VSM measurements were repeated at least twice for each processing condition. When anomalously soft hysteresis loops or magnetic responses inconsistent with the expected behavior were observed, additional measurements were performed to assess reproducibility and investigate potential sample-related or experimental effects. Such behavior was considered potentially consistent with oxidation-related degradation; however, oxidation was not assumed to be the definitive cause in the absence of direct evidence. The reproducibility between repeated measurements was ±10 kA m^{-1} for H_c and ±1 A·m^2/kg for M_r and M(1700 kA m^{-1}).

3. Results and Discussion

3.1. Characterization of the Recycled Powders After HPMS and Jet Milling

The demagnetization curve of a collected EoL reference magnet revealed a B_r of 1.33 T, a H_{cj} of 1401 kA/m, and a $(BH)_{max}$ of 298 kJ/m^3. After hydrogen processing and subsequent jet milling to reduce the particle size, the composition of the recycled milled powder was

analyzed using ICP-OES, and the results are presented in Table 2. The chemical analysis revealed the presence of several additives, in order of percentage: Dy (4.17 wt.%), Al (0.46 wt.%), Si (0.20 wt.%), Pr (0.11 wt.%), Cu (0.06 wt.%), Nb, Cr and Sn (0.02 wt.% each), and Tb, Ga, Ce, and Ni (0.01 wt.% each), as well as the three primary constituents: Nd (27.60 wt.%), Fe (64.78 wt.%), and B (1 wt.%). These results are consistent with the typical composition of commercial NdFeB magnets.

Table 2. ICP-OES measurements of the HPMS jet-milled powder. Note: The sum of the reported elemental concentrations was 98.48 wt.%. The balance (~1.5 wt.%) corresponds mainly to light elements that cannot be determined by ICP-OES, namely, O, H retained in the hydrided powder, and N from milling in N_2 and C, together with the analytical uncertainty of the major elements. Other metallic elements were below 0.01 wt.%.

	Element (wt. %)															
Sample	**Nd**	**Fe**	**Dy**	**B**	**Pr**	**Al**	**Si**	**Cu**	**Nb**	**Tb**	**Ga**	**Ce**	**Cr**	**Sn**	**Ni**	**Total**
HPMS JM	27.60	64.78	4.17	1	0.11	0.46	0.20	0.06	0.02	0.01	0.01	0.01	0.02	0.02	0.01	98.48

Rare-earth substituents such as the heavy rare earth (HRE) Dy and the light rare earth (LRE) Pr are common in these magnets. Dy raises the anisotropy field and, therefore, the coercivity and thermal stability, at the cost of a lower remanence when it is alloyed into the bulk. Grain boundary diffusion processes concentrate Dy in shells around the $Nd_2Fe_{14}B$ grains and reduce this penalty. The Dy content of ~4 wt.% is consistent with the high-coercivity grades used in wind-turbine generators [22,48–50]. Conversely, Pr originates from the Nd precursor, and it helps to reduce production costs [51]. It is also added (due to its easy substitution for Nd at the surface of the grains and easy diffusion in the magnet) to increase the anisotropy field and, consequently, enhance the coercivity [52]. Small additions of other elements, including Cu, Ga, Si, and Al, are known to promote improved wetting of the GBP, thereby improving coercivity [53]. Other minor additions of Ce, Cr, and Sn were found in the composition, elements that are usually incorporated in NdFeB [54–56].

Backscattered-electron (BSE) SEM images of the EoL reference magnet, the HPMS powder, and the HPMS jet-milled powder are shown in Figure 2. Figure 2a represents the typical microstructure of a NdFeB magnet, consisting of a matrix phase of $Nd_2Fe_{14}B$ (gray areas) and smaller particles corresponding to the Nd-rich phases (brighter contrast areas) located at the grain boundaries. Figure 2b shows the morphology of the powder after hydrogen decrepitation (HPMS). This process creates stress, causing the material to fracture and break down into smaller particles, forming a friable material [57]. Interestingly, crack propagation occurs along grain boundaries, which indicates a relevant role of grain boundaries in hydrogen processing. Finally, Figure 2c illustrates the structure of the hydrogenated powder after jet milling. As can be seen, the particle size decreased and the particles deagglomerated.

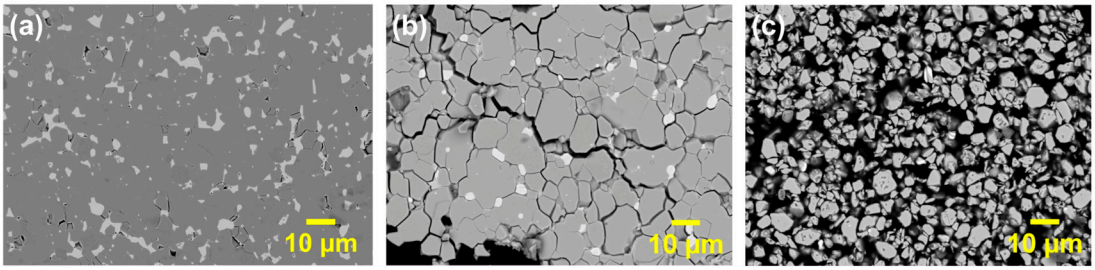


Figure 2. BSE-SEM images of the (**a**) starting EoL magnet and recycled powder after (**b**) HPMS and (**c**) subsequent jet milling in N_2.

Figure 3a illustrates a higher-magnification (×2000) backscattered SEM image of HPMS powder, revealing its distinctive fragmented microstructure, produced by hydride formation, first in the Nd-rich grain boundary phase and then in the matrix, which generates intergranular and transgranular cracks that pulverize the magnet [32]. However, it is important to mention that incomplete propagation along grain boundaries may result in multi-grain fragments with reduced alignment. This characteristic friability facilitates the subsequent reduction to single-grain particles by jet milling, as can be seen in Figure 3d. Single-grain particles favor alignment during compaction and a higher coercivity in the final magnet. Figure 3b,e show EDS analyses in selected positions to study the phases present in the sample. The elemental compositions obtained by EDS at various locations are summarized in Table 3. Three distinct regions (p1–p3) were identified in the HPMS powder. The composition at p1 (~72 wt.% Fe and ~24 wt.% Nd) corresponds to the $Nd_2Fe_{14}B$ matrix phase, which is consistent with the expected stoichiometry for the hard magnetic phase. In contrast, regions p2 and p3 exhibited strong enrichment in Nd (76 wt.% and 60 wt.%, respectively) with high oxygen levels (14 wt.% and 16 wt.%, respectively), with minor Fe content (2 wt.% in p2 and 23 wt.% in p3) and Dy only detected in p2 with a content of 8.6 wt.%. These areas are indicative of oxidized Nd-rich grain boundary phases, formed after the HPMS process. After jet milling (HPMS JM), two representative regions were analyzed. Region p1 exhibited a composition similar to the $Nd_2Fe_{14}B$ matrix (~71.6 wt.% Fe, ~23.8 wt.% Nd, and ~4.4 wt.% Dy), confirming the chemical stability of the bulk magnetic phase after milling. However, region p2 showed a pronounced enrichment in Nd (71.8 wt.%) and oxygen (19.6 wt.%), alongside a reduction in Fe (2.5 wt.%). This suggests that the oxidation of the Nd-rich boundary phase was enhanced by the high specific surface area and localized heating during milling. Traces of Al (<1 wt.%) can be observed in the analysis. A minor spurious signal at 2.31 keV originally attributed to sulfur has been excluded, as the ICP-OES bulk analysis (Table 2) shows no measurable S. The EDS signal is most likely due to peak overlap between S Kα (2.309 keV) and Mo Lα (2.293 keV, from the sample holder), and/or polishing residues (see note to Table 3).

Table 3. Chemical composition (wt.%) at different locations in the HPMS, HPMS jet-milled (JM), and HPMS JM degassed powders obtained by EDS point analysis. Note: A minor EDS signal originally assigned to S has been excluded from this table because it was not confirmed by ICP-OES bulk analysis (Table 2). The signal is most likely due to Mo Lα/S Kα peak overlap (2.293 vs. 2.309 keV) or to polishing-residue contamination.

	HPMS			**HPMS JM**		**HPMS JM Degassed**	
Element (wt.%)	**p1**	**p2**	**p3**	**p1**	**p2**	**p1**	**p2**
Al	0.33	-	-	0.27	-	0.33	-
Fe	72.12	2.11	22.91	71.55	2.54	70.08	1.71
Nd	23.65	75.71	60.33	23.78	71.77	24.91	78.70
Dy	3.91	8.57	-	4.41	6.10	4.56	6.01
O	-	13.61	16.12	-	19.60	-	13.58
Si	-	-	-	-	-	0.13	-

Figure 3c,f show the grain and particle size distributions of the HPMS and HPMS JM powders, respectively, which were calculated from the SEM micrographs. Both distributions were fitted to lognormal functions. The grain size distribution of the HPMS powder is described by the lognormal parameters $\mu = 1.54$ and $\sigma = 0.57$ (ln μm), corresponding to a mean equivalent diameter of 5.5 ± 3.4 μm (mean ± standard deviation of the distribution). The jet-milled powder shows a lower and narrower distribution ($\mu = 1.09$, $\sigma = 0.40$), with a mean particle diameter of 3.2 ± 1.3 μm. This reduction in mean size and dispersion confirms

the effectiveness of jet milling in refining the powder and producing a more homogeneous particle size distribution.

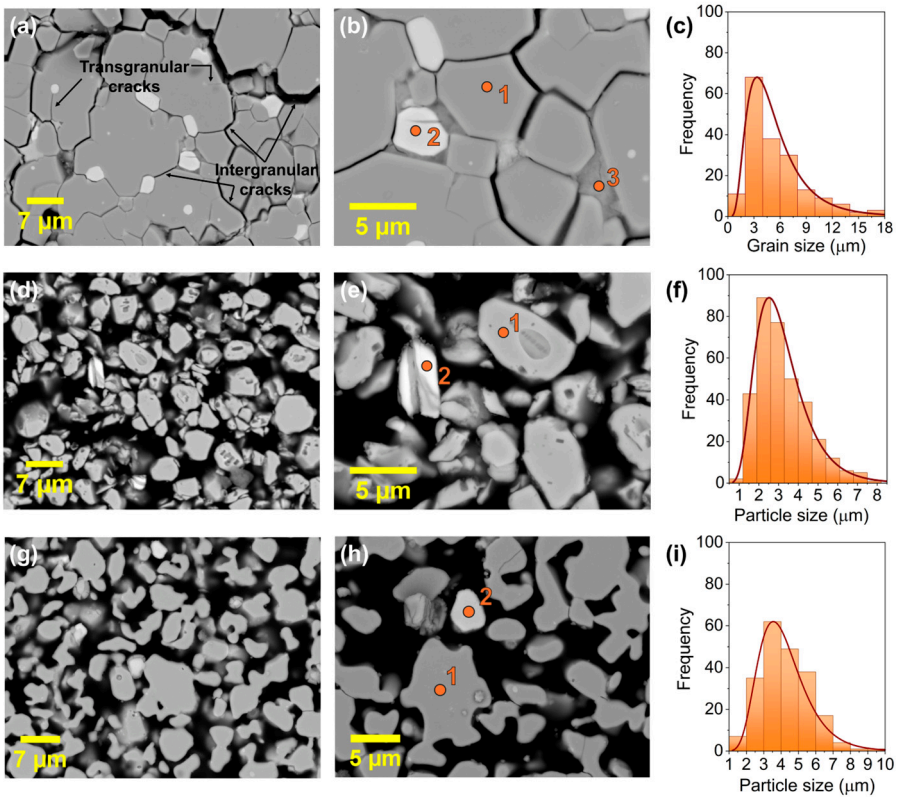


Figure 3. BSE-SEM micrographs at 2000× magnification showing the microstructure of (**a**) the HPMS powder, (**d**) the HPMS jet-milled (JM), and (**g**) HPMS JM degassed powders. The gray regions correspond to the NdFeB matrix phase, while the white areas correspond to the Nd-rich phases. Intergranular and transgranular cracks in the HPMS powder are marked with black arrows. (**b**,**e**,**h**) The BSE-SEM images of the samples at 5000× magnification, indicating where EDS point analysis was performed (points marked in orange). (**c**) Grain size distribution of the HPMS powder and particle size distribution of (**f**) the HPMS JM and (**i**) the HPMS JM degassed powders calculated from the SEM images. The cumulative distribution curve is displayed in brown.

As shown in the BSE-SEM images (Figure 3g) and confirmed by EDS analysis at different locations in Figure 3h, the degassed powder exhibits a typical NdFeB microstructure, consisting of a $Nd_2Fe_{14}B$ matrix phase (gray contrast) and Nd-rich phases (bright contrast), as previously observed in the hydrogenated powders. The EDS results (Table 3) reveal that the main matrix phase (p1) is rich in Fe (~70 wt.%) and contains around 25 wt.% of Nd, while the bright regions (p2) are enriched in Nd (~79 wt.%) and present approximately 14 wt.% of oxygen, corresponding to oxidized Nd-rich boundary phases. Traces of Al and Si (<0.5 wt.%) can be found in the compositional analysis.

After the degassing treatment at 900 °C, a moderate increase in the average particle size of the HPMS jet-milled powder was observed. The particle size distribution (Figure 3i), determined from the SEM images and fitted to a lognormal function ($\mu = 1.38$, $\sigma = 0.34$), indicates a mean particle size of 4.2 ± 1.5 µm, resulting in a slight coarsening and a partial coalescence of the particles in comparison with the as-milled HPMS powder, whose average particle diameter was of around 3.2 µm.

SEM analysis of the HPMS jet-milled powder revealed the presence of a thin oxide layer of the order of 0.1 µm on the edges of some particles, as can be seen in Figure 4a. This feature, together with the slightly higher oxygen content measured by elemental analysis (0.59 wt.% compared to 0.46 wt.% in the unmilled powder), suggests enhanced surface oxidation

during the high-energy milling process. As reflected in Figure 4b, the formation of this oxide layer is expected to influence the magnetic performance. Despite a moderate increase in both M(1700 kA m^{-1}) (from 113 to 126 A·m^2/kg) and remanent magnetization (from 10.0 to 10.5 A·m^2/kg), there is an observed decrease in coercivity (from 38.7 to 28.0 kA/m), see Table 4. This phenomenon has been reported in the literature [57], where H_c decreases with further grain refinement when the grain size is below a critical value. In line with the findings of Li et al. [21], the threshold value was found to be 3.5 µm, with an enhancement in H_c only observed within the 3.5–7.5 µm range. The increase in magnetization can be attributed to the removal or fragmentation of non-magnetic Nd-rich surface phases, which results in a greater volume fraction of the $Nd_2Fe_{14}B$ matrix being exposed. Therefore, although jet milling effectively refines particle size and enhances magnetic phase exposure, it also promotes surface oxidation, which degrades the hard magnetic response of the recycled powder.

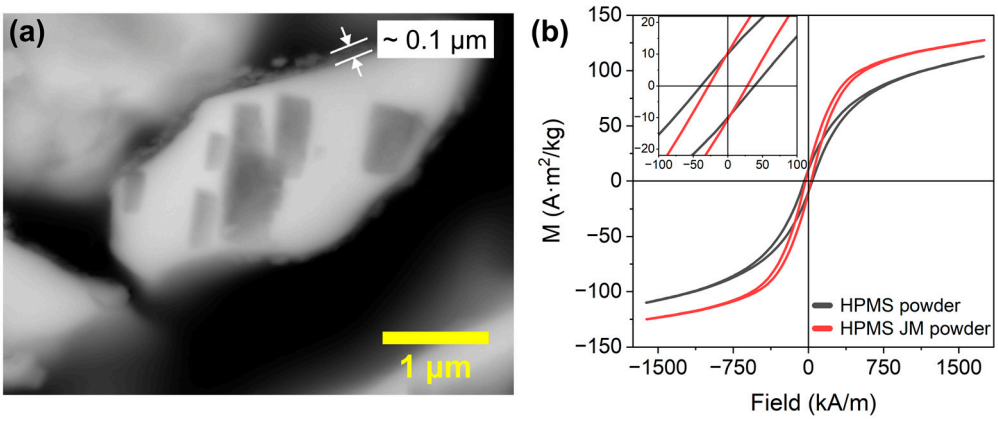


Figure 4. (**a**) BSE-SEM image of the HPMS jet-milled powder showing a thin layer (~0.1 µm) of oxidation on the grains indicated by white arrows. (**b**) Hysteresis curves of the recycled powder after HPMS and jet milling.

Table 4. Magnetic properties (coercivity, H_c, remanence, M_r, and magnetization at maximum applied field, M(1700 kA m^{-1})) and oxygen content of the HPMS non-milled, jet-milled, and degassed (DG900-2) powders. The oxygen content of DG900-2 is the mean ± standard deviation of three specimens.

Samples	H_c (kA/m)	M_r (A·m²/kg)	M(1700 kA m^{-1}) (A·m²/kg)	O (wt.%)
HPMS non-milled powder	38.7	10.0	113	0.46
HPMS jet-milled powder	28.0	10.5	126	0.59
Degassed powder (DG900-2)	434.1	53.1	87.7	0.66 ± 0.06

It should be noted that the ~27% reduction in coercivity produced by jet milling can be due to reasons different than oxygen uptake alone. Two additional mechanisms, activated by the jet-milling impacts, can contribute. First, by introducing surface defects, dislocations, and residual stress layers, which act as nucleation sites for reverse domains and are known to reduce the coercivity of NdFeB powders. Second, partial disruption of the Nd-rich grain boundary phase, as jet milling preferentially breaks along the softer intergranular layer, exposing fresh $Nd_2Fe_{14}B$ surfaces and degrading the continuity of the non-magnetic pinning layer that provides magnetic isolation between grains.

3.2. Characterization of the Degassed Powders

3.2.1. Desorption Kinetics

After jet milling, degassing was performed on the hydrogenated powders via vacuum heat treatment, aimed at eliminating H_2 from the structure and restoring the magnetic properties of the recycled powders. To compare the desorption behavior across conditions, Figure 5 shows the deconvolution of two desorption curves, corresponding to $\beta = 3$ °C/min (DG800-3) and $\beta = 2$ °C/min (DG900-2). The three-Gaussian deconvolution reproduced the experimental desorption profiles with excellent agreement ($R^2 = 0.999$), allowing the overlapping contributions to be resolved and compared across the investigated conditions. The first peak (A) was deconvoluted and corresponds to the combination of two desorption processes: (A_1) and (A_2), associated, respectively, with the release of hydrogen from the $Nd_2Fe_{14}BH_x$ hard magnetic phase at ~150 °C (A_1), and at ~230 °C with the transformation of $NdH_{2.7}$ to NdH_2 in the grain boundary phase [58,59]. Finally, the smallest degassing peak (B) at higher temperature (~530 °C) represents the dehydrogenation of a more stable hydride species, specifically the NdH_2 secondary phase, resulting in the formation of metallic Nd [41,58]. Hydrogen is removed at higher temperatures for the neodymium hydrides due to their stability.

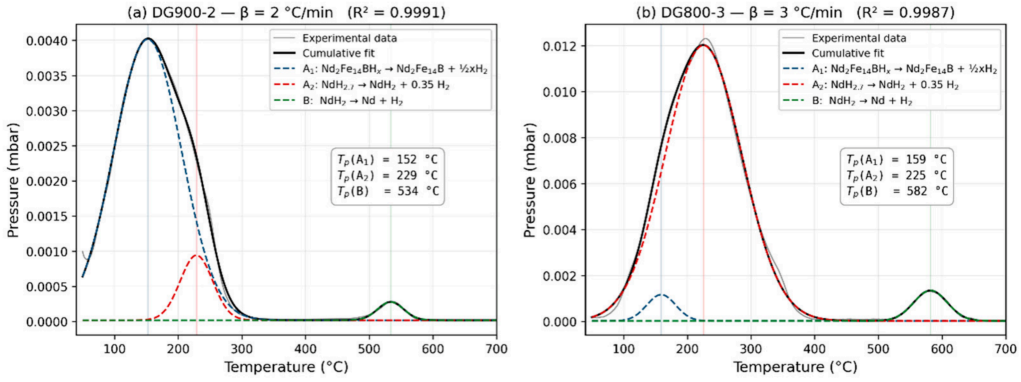


Figure 5. Desorption curves and corresponding Gaussian deconvolution of the hydrogen desorption traces of HPMS jet-milled NdFeB powders at (**a**) $\beta = 2$ °C/min (sample DG900-2, $T_{max} = 900$ °C) and (**b**) $\beta = 3$ °C/min (sample DG800-3, $T_{max} = 800$ °C). The three-Gaussian fits yielded a coefficient of determination of $R^2 = 0.999$. The assignment of the components is based on data from the literature [44,58,59]. The gray curves are the smoothed experimental data, and the black solid line is the cumulative three-Gaussian fit. The deconvoluted sub-peaks correspond to the three desorption processes: A_1, hydrogen release from the $Nd_2Fe_{14}BH_x$ main phase (blue dashed); A_2, partial decomposition of the $NdH_{2.7}$ grain boundary phase to NdH_2 (red dashed); B, full decomposition of NdH_2 to metallic Nd (green dashed). The three deconvoluted desorption reactions are A_1: $Nd_2Fe_{14}BH_x \rightarrow Nd_2Fe_{14}B + (x/2)\ H_2$; A_2: $NdH_{2.7} \rightarrow NdH_2 + 0.35\ H_2$; B: $NdH_2 \rightarrow Nd + H_2$.

All three peaks, typical of NdFeB dehydrogenation [60,61], shift to higher temperature as the heating rate increases from 2 to 3 °C/min, in the direction predicted by the Kissinger relation [62], which supports the reproducibility of the three-component decomposition across heating rates. Because the heating rate window is too narrow for a Kissinger analysis, the activation energies were estimated from the $\beta = 2$ °C/min trace with the Redhead approximation [46] (Equation (1)):

$$E_a = R \cdot T_p \cdot [\ln(\nu \cdot T_p/\beta) - 3.64], \quad (1)$$

where R is the gas constant, T_p is the peak temperature in K, β is the heating rate in K s^{-1}, and ν is the pre-exponential (attempt) factor of the assumed first-order desorption process. Following the standard convention for atomic and small-molecule desorption from solids [46],

values of $\nu = 10^{13}$ s^{-1} and $\nu = 10^{11}$ s^{-1} were used to bracket the range commonly reported for hydrogen desorption from metal hydrides. For $\nu = 10^{13}$ s^{-1}, $\nu/\beta \approx 3 \times 10^{14}$ K^{-1} lies above the range (10^{8}–10^{13} K^{-1}) for which Redhead established the accuracy of Equation (1) [46]. The values in Table 5 were, therefore, obtained by solving numerically the exact peak-maximum condition for first-order desorption,

$$E_a/(RT_p^2) = (\nu/\beta)\cdot\exp(-E_a/RT_p) \quad (2)$$

they differ from those given by Equation (1) by less than 1 kJ mol^{-1}.

Table 5. Activation energies E_a for the three deconvoluted desorption sub-processes of the HPMS jet-milled NdFeB powder, estimated for first-order desorption from the $\beta = 2$ °C/min trace (sample DG900-2, Figure 5a). The two columns correspond to two limiting values of the assumed pre-exponential factor ν, bracketing the range typically reported for hydrogen desorption from metal hydrides. E_a was calculated using Equation (2); the Redhead approximation (Equation (1)) gives values within 1 kJ mol^{-1}.

Sub-Peak	Assignment	T_p (°C)	E_a (kJ/mol), $\nu = 10^{13}$ s^{-1}	E_a (kJ/mol), $\nu = 10^{11}$ s^{-1}
A_1	$Nd_2Fe_{14}BH_x \rightarrow Nd_2Fe_{14}B + (x/2)H_2$	152	127	111
A_2	$NdH_{2.7} \rightarrow NdH_2 + 0.35H_2$	229	150	131
B	$NdH_2 \rightarrow Nd + H_2$	534	245	214

As discussed in Section 2.2, these E_a values are approximate, and the interpretation relies on their relative ordering $E_a(A_1) < E_a(A_2) < E_a(B)$ rather than on their absolute values.

The E_a values exhibit the expected ordering $E_a(A_1) < E_a(A_2) < E_a(B)$, consistent with the relative binding strengths of the three hydride states. The values for peaks A_1 ($Nd_2Fe_{14}BH_x \rightarrow Nd_2Fe_{14}B + (x/2)H_2$, ~111–127 kJ/mol) and A_2 ($NdH_{2.7} \rightarrow NdH_2 + 0.35H_2$, ~131–150 kJ/mol) are in the range previously reported for hydrogen desorption from $Nd_2Fe_{14}B$ and from Nd-rich grain boundary phases [58]. The activation energy for peak B ($NdH_2 \rightarrow Nd + H_2$, ~214–245 kJ/mol) is lower than typical literature values for the bulk NdH_2 decomposition, which may reflect the higher specific surface area of the jet-milled HPMS samples studied here.

3.2.2. Magnetic Characterization

Figure 6 presents the magnetic characterization of recycled NdFeB powders subjected to various heat treatment conditions aimed at degassing, with particular focus on the influence of temperature and heating rate. Table 6 summarizes the main magnetic parameters. As noted in Section 2.5, the loops are not fully saturated, so H_c, M_r, and M(1700 kA m^{-1}) are lower limits—the comparison between samples measured under the same conditions remains valid. Specifically in Figure 6a, the hysteresis loops of samples treated at different temperatures (650, 800, and 900 °C) with a constant heating rate of 3 °C/min (DG650-3, DG800-3, and DG900-3) reveal a progressive decrease in M(1700 kA m^{-1}) with increasing temperature. H_c shows a clear increase at 900 °C. A possible explanation for this observation comes from the fact that the reduction of surface defects on the grains activated by temperature is known to minimize potential nucleation sites for reversed magnetic domains in NdFeB, thereby preserving coercivity [63]. In contrast, Figure 6b compares degassed samples treated at 900 °C with varying heating rates (1, 2, and 3 °C/min), and shows that H_c is similar for $\beta = 1$ and 2 °C/min (430.8 and 434.1 kA/m, a difference below 1%) and lower for $\beta = 3$ °C/min (361.9 kA/m), whereas M(1700 kA m^{-1}) is highest for $\beta = 2$ °C/min (87.7 A·m^2/kg, compared with 73.7 and 80.9 A·m^2/kg for $\beta = 1$ and 3 °C/min). Two caveats apply: the 1 °C/min sample was held for 60 min instead of 10 min, and the 3 °C/min sample in Figure 6b (DG900-3*) was held for 5 min, so heating rate and time at temperature are not fully decoupled in this series. With these caveats, 2 °C/min gave the best overall balance.

A plausible interpretation is that slow ramps prolong the exposure of the fine powder to residual oxygen at high temperature, whereas fast ramps leave less time for hydrogen release and recombination. Dwell-time-matched experiments are needed to test this hypothesis. A partial decoupling based on the existing data is presented below (Figure 7).

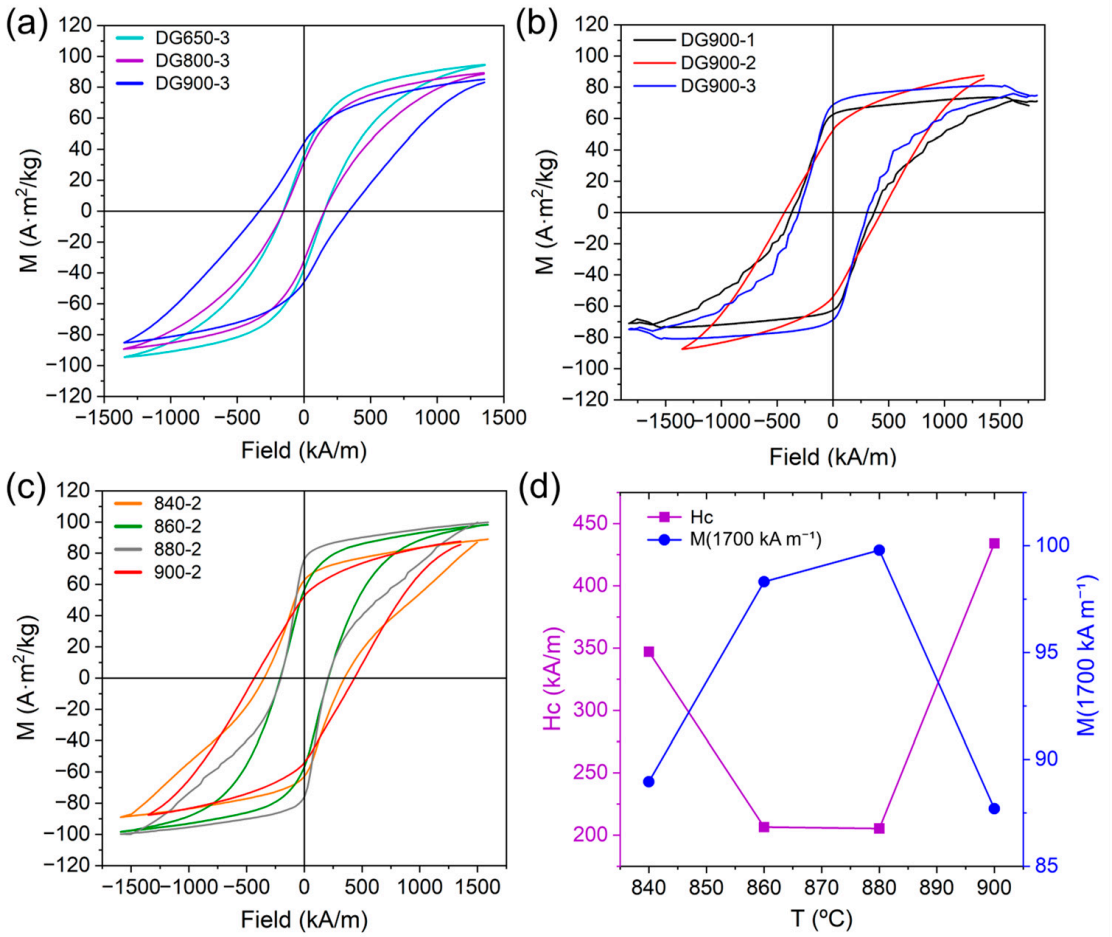


Figure 6. Magnetic hysteresis curves at room temperature (RT) of the degassed powders obtained after a heat treatment at different temperatures and heating rates: (**a**) 650, 800, and 900 °C with a heating rate of 3 °C/min, (**b**) 900 °C with heating rates of 1, 2, and 3 °C/min (DG900-3*, 5 min dwell), (**c**) a ramp of 2 °C/min at degassing temperatures of 840, 860, 880, and 900 °C, and (**d**) H_c and $M(1700\ \text{kA m}^{-1})$ as a function of degassing temperature for $\beta = 2$ °C/min.

Table 6. Degassing conditions and magnetic properties of the degassed powders. The sample marked with an asterisk was held for 5 min at 900 °C and is shown in Figure 6b; DG900-3, held for 10 min, is shown in Figure 6a. H_c, M_r, and $M(1700\ \text{kA m}^{-1})$ are lower limits (Section 2.5).

Sample	Degassing Temperature (°C)	Heating Rate (°C/min)	Dwell Time (min)	H_c (kA/m)	M_r (A·m²/kg)	$M(1700\ \text{kA m}^{-1})$ (A·m²/kg)
DG900-1	900	1	60	430.8	62.7	73.7
DG840-2	840	2	10	347.1	62.8	89.0
DG860-2	860	2	10	206.5	56.6	98.3
DG880-2	880	2	10	205.4	76	99.8
DG900-2	900	2	10	434.1	53.1	87.7
DG650-3	650	3	10	155.0	37.0	94.6
DG800-3	800	3	10	152.8	31.9	89.3
DG900-3	900	3	10	336.3	45.1	85.2
DG900-3*	900	3	5	361.9	68.7	80.9

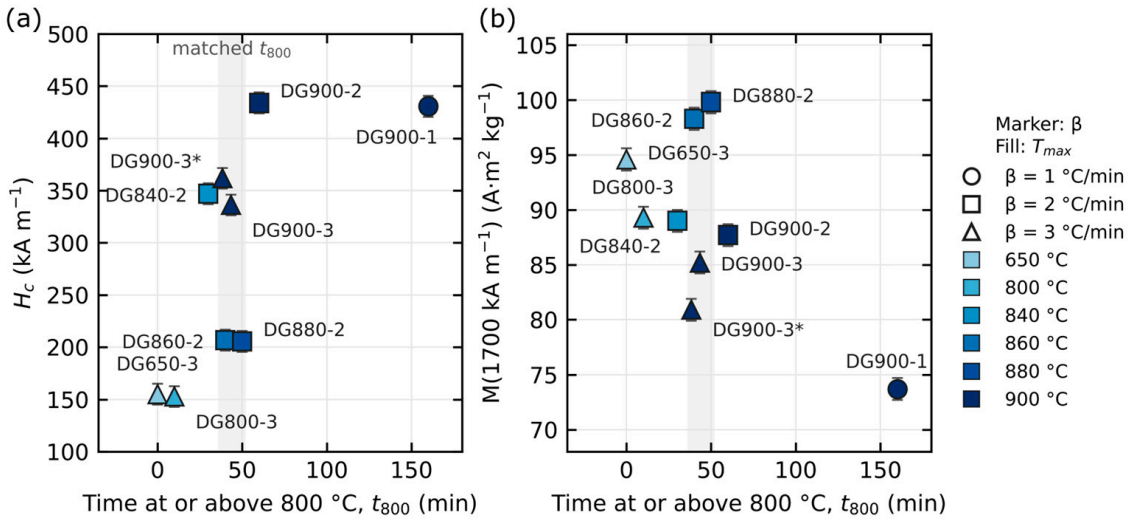


Figure 7. (**a**) Coercivity H_c and (**b**) M(1700 kA m^{-1}) of the degassed powders as a function of the time spent at or above 800 °C, $t_{800} = (T_{max} - 800\ °C)/\beta + t_{dwell}$, calculated from the conditions in Table 6 (furnace cooling not included). Marker shape indicates the heating rate β and fill color the degassing temperature T_{max}. The shaded band marks conditions with comparable t_{800} (38–50 min). Error bars show the reproducibility of repeated measurements (±10 kA m^{-1} for H_c, ±1 A·m^2/kg for M(1700 kA m^{-1})).

Figure 6c further explores the effect of temperature at a fixed rate of 2 °C/min. Considering that the most favorable properties were initially obtained at 900 °C, an in-depth study was conducted at close temperatures to optimize the degassing process. This included temperatures of 840 °C, 860 °C, 880 °C, and 900 °C. Results show that sample DG900-2 (red curve) exhibits a more open loop with higher H_c but reduced remanence, M_r = 53.1 A·m^2/kg. Sample DG840-2 (orange curve) shows a relatively squared loop similar to the sample treated at 900 °C, but narrower in the center. At intermediate temperatures, 860 and 880 °C, samples present a softer magnetic response, but M(1700 kA m^{-1}) is enhanced. Figure 6d summarizes the dependence of coercivity and M(1700 kA m^{-1}) with temperature at 2 °C/min, highlighting the inverse relationship between H_c and M(1700 kA m^{-1}). Coercivity decreases at intermediate temperatures, while M(1700 kA m^{-1}) reaches its maximum value (99.8 A·m^2/kg at 880 °C). On the contrary, maximum values of H_c = 434.1 kA/m are obtained for the highest-temperature treatment, at 900 °C, followed by the lowest-temperature treatment, at 840 °C, with a value of 347.1 kA/m, with M(1700 kA m^{-1}) values of 87.7 A·m^2/kg and 89 A·m^2/kg, respectively.

Because heating rate and time at temperature are coupled in the heating rate series, the magnetic data were also examined against the time spent at or above 800 °C, t_{800} (Section 2.2), which ranges from 0 min (DG650-3) to 160 min (DG900-1; Figure 7). Coercivity is not ordered by t_{800}. At comparable t_{800} (38–50 min, shaded band in Figure 7a), the samples degassed at 900 °C (DG900-3 and DG900-3*, H_c = 336–362 kA/m) show 1.6–1.8 times the coercivity of those degassed at 860 and 880 °C (DG860-2 and DG880-2, $H_c \approx$ 206 kA/m). The comparison does not depend on the choice of threshold: for 850 °C, for example, DG880-2 and DG900-3 spent 25 and 27 min above the threshold and reached H_c = 205 and 336 kA/m, respectively. Within the 900 °C series, H_c increases from 336–362 kA/m at $t_{800} \approx$ 40 min to 434 kA/m at 60 min and does not increase further at 160 min (431 kA/m, DG900-1). The lower coercivity at 3 °C/min is, therefore, consistent with an insufficient time above 800 °C, and extending this time beyond about 60 min brings no further gain in H_c. M(1700 kA m^{-1}), in contrast, is lowest for the longest exposure (DG900-1, 73.7 A·m^2/kg after about 15.6 h of heating and dwell, of which 11 h above 300 °C; Figure 7b), consistent with, but not proof of,

a progressive degradation of the powder during long thermal exposure. This analysis does not replace dwell-matched experiments and cannot separate an effect of the heating rate itself from that of the time spent above 800 °C. It does indicate that, in the range investigated, coercivity depends primarily on the peak degassing temperature (non-monotonically, as discussed below) rather than on the time spent above 800 °C, so the degassing window identified here does not rest on the heating rate comparison alone.

Tying together the desorption and magnetic data, the peak temperature of 534 °C at $\beta = 2$ °C/min (582 °C at 3 °C/min) sets the practical lower bound on the degassing window: the NdH_2 desorption peak (B) is completed only above about 600 °C at 2 °C/min and 630 °C at 3 °C/min (Figure 5), so treatments ending below these temperatures would be expected to leave hydrogen in the grain boundary phase. This bound is inferred from the desorption traces and was not verified by a direct hydrogen measurement (Section 3.3). In addition, it is known that the HPMS process can lead to the formation of α-Fe through localized disproportionation [30,41], which lowers coercivity and raises magnetization. This is consistent with a parallel work, on HPMS NdFeB powder of comparable (though not identical) origin, in which we have observed by Mössbauer spectroscopy (Mössbauer spectra were recorded at 298 K and 8 K in the transmission mode using a closed-cycle He cryogenerator and a conventional constant acceleration spectrometer equipped with a ^{57}Co(Rh) source) the formation of α-Fe after the HPMS process, supporting this as a likely hypothesis rather than a confirmed mechanism for the specific powders studied here [64]. In order to recover NdFeB coercivity, recombination of Fe with NdH_2, which is known to happen in the 800–900 °C range [30], should be activated. Indeed, the sample degassed at 650 °C presents high M(1700 kA m^{-1}) and low H_c, consistent with the presence of α-Fe in the sample. As the degassing temperature increases, Fe is expected to recombine with NdH_2, which would account for the H_c values converging toward NdFeB coercivity.

We cannot discard that oxygen uptake during the degassing treatment influences the coercivity of the recovered powder. Three specimens degassed at 900 °C with $\beta = 2$ °C/min contained 0.66 ± 0.06 wt.% O (mean ± standard deviation), compared with 0.46 wt.% after HPMS and 0.59 wt.% after jet milling (Table 4). The increase after degassing (~0.07 wt.%) is comparable to the specimen-to-specimen scatter, so the data do not establish whether additional oxygen was taken up during the thermal treatment or whether the difference arises from handling and sampling. All values are well above the ~0.1 wt.% targeted in low-oxygen processing of high-performance magnets, although below the ~1 wt.% above which marked degradation was reported for metal-injection-molded magnets made from recycled powders [65]. Oxygen, therefore, remains a key limitation of the present route. Two aspects of our work suggest that severe additional oxidation is unlikely to dominate the observed behavior, without excluding a partial contribution. First, the degassing is performed under a dynamic vacuum of 10^{-3}–10^{-5} mbar throughout the entire heating cycle, which limits the oxygen partial pressure; however, at $\beta = 2$ °C/min the powder spends several hours above 300 °C, so the exposure is not limited to the 10 min dwell. Second, the coercivity recovery observed at 900 °C (H_c = 434.1 kA/m, an order of magnitude above the as-milled value of 28.0 kA/m) would be difficult to reconcile with severe additional oxidation of the Nd-rich grain boundary phase, since such oxidation would be expected to suppress, rather than assist, the recombination process invoked to restore H_c. Even so, a moderate oxidation of the grain boundary phase at the highest degassing temperatures, contributing to an imperfect coercivity recovery, remains a plausible possibility that we cannot rule out with the data at hand.

To interpret the non-monotonic dependence visible in Figure 6c,d, we propose, as a plausible hypothesis rather than a confirmed picture, that at 900 °C the recombination of α-Fe with dehydrogenated Nd to reform the $Nd_2Fe_{14}B$ main phase would be close to completion,

α-Fe largely consumed, and both loop squareness and Hc close to their maximum values. At 860–880 °C, recombination would not yet be complete within the 10 min dwell, so that residual α-Fe could still be present, which would lower H_c while raising $M(1700\ \text{kA m}^{-1})$, tentatively consistent with the poorer squareness of these loops in Figure 6c. The behavior at 840 °C is less straightforward: Zakotnik et al. [41] reported an analogous anomaly in H_c and B_r in this temperature range on sintered HD powder and attributed it to the onset of partial exchange-coupling between residual Fe and the surrounding $Nd_2Fe_{14}B$ grains activated at these temperatures. Such graded/imperfect exchange coupling is known to enhance both H_c and B_r at low coupling strength and to lead to domain-wall propagation and magnetic softening as the coupling strength increases [66–68]. This mechanism could explain the higher H_c observed at 840 °C relative to 860–880 °C. We caution, however, that since our loops are minor loops measured below full saturation, fluctuations in the degree of particle alignment, an effect also invoked by Zakotnik et al. [41], could produce the same signature. Direct verification, in particular by XRD or Mössbauer spectroscopy quantifying the α-Fe volume fraction across the degassing series, would be needed to distinguish between these possibilities and is planned as a follow-up to this work.

Regarding the practical implications of the absolute coercivity level, the best value reported here, $H_c = 434$ kA/m, is well below the 1401 kA/m of the original sintered EoL magnet. Three factors contribute to this difference: (i) the VSM measurements were performed at a maximum applied field ($1700\ \text{kA m}^{-1}$) below the full saturation field of the recycled powder, so the reported H_c represents a lower limit of the intrinsic coercivity, as already noted, (ii) the degassed powder is fine, jet-milled and unbonded, and sintered magnets derive part of their coercivity from the exchange-decoupling geometry created during sintering and the associated grain boundary phase redistribution, which is absent here, and (iii) the residual α-Fe hinted at by the $M(1700\ \text{kA m}^{-1})$ trend discussed above reduces the effective coercivity even at the optimum degassing condition. With respect to bonded magnets, the best coercivity obtained here remains below the $\geq$600 kA m^{-1} typical of commercial isotropic bonded-magnet powders [69], which owe their coercivity to a nanocrystalline microstructure. In its present state, the degassed powder, therefore, does not meet the requirements of high-performance bonded magnets. Lower oxygen contents, complete recombination, and restoration of the grain boundary phase (for example by Nd-rich additions [65]) would be needed, and blending with primary powder is a possible intermediate option.

Comparing our optimal degassing temperatures with the existing bibliography, Zakotnik et al. [41,70] reported that optimal degassing occurred at around 700 °C for powders used in sintered magnet processing. Other studies in the literature have successfully removed hydrogen by degassing at 600 °C for 2 h under vacuum [27,61]. S. Rathfelder et al. [43] employed these degassing conditions to produce anisotropic NdFeB permanent magnets via powder extrusion molding (PEM). In all these cases, a subsequent high-temperature (sintering most commonly) treatment took care of the recombination and yielded the appropriate composition and microstructure. For routes without a later sintering step, such as polymer-bonded magnets, the degassing treatment must itself achieve both hydrogen desorption and the recombination of the $Nd_2Fe_{14}B$ phase, which requires higher temperatures. Consequently, the optimal magnetic parameters and thermal windows differ significantly, highlighting the importance of tailoring the degassing protocol to the specific intended application of the recycled powder.

The thermal degassing profile, particularly the peak degassing temperature and the associated time at temperature, therefore, plays a pivotal role in tailoring coercivity and $M(1700\ \text{kA m}^{-1})$. The trade-off observed between H_c and $M(1700\ \text{kA m}^{-1})$, particularly at

certain temperatures, suggests that selecting the appropriate thermal conditions depends on the specific starting EoL material and the application requirements.

3.3. Scope and Limitations of the Present Study

The aim of this work is to identify, for a real EoL feedstock, the degassing conditions that recover the magnetic properties of HPMS jet-milled powder when no later sintering step is available. The degassing window is, therefore, defined by a functional criterion, the measured H_c and M(1700 kA m^{-1}) of the degassed powder, and the desorption traces are used to bound it. Three limitations of the dataset should be considered when using these results.

First, the hydrogen content of the powder was not measured before or after degassing. The evidence for hydrogen removal is indirect but consistent: (i) The desorption traces show the three expected components and return to the baseline above about 600 °C (2 °C/min) and 630 °C (3 °C/min), with no further desorption detected up to 700 °C (Figure 5). (ii) The degassing temperatures of the window (840–900 °C) lie at least 250 °C above the last desorption peak and coincide with the conditions of the desorption–recombination stage of HDDR processing, in which NdH_2 is decomposed under vacuum [30,58]. (iii) The coercivity increases from 28.0 kA/m after jet milling to 153–434 kA/m after degassing (Tables 4 and 6), as expected when the magnetocrystalline anisotropy reduced by hydrogen in $Nd_2Fe_{14}BH_x$ is restored [26,27]. The location of the window rests on the measured magnetic response, not on an assumed hydrogen content, and H_c changes markedly between 840 and 900 °C, a range in which no desorption is detected. Residual hydrogen below the detection limit of the pressure trace cannot be excluded—a direct measurement by inert-gas fusion would quantify it and is part of the follow-up work.

Second, heating rate and time at temperature were coupled in the heating rate series. The thermal-budget analysis of Figure 7 separates them only partially, but it shows that, at comparable time above 800 °C, coercivity depends primarily on the peak degassing temperature. The temperature window itself was obtained at a fixed heating rate and does not depend on this coupling—the choice of 2 °C/min should be read as the best of the conditions tested, not as a general optimum.

Third, the roles of α-Fe recombination and of oxidation are presented as hypotheses. All conditions were run on powder from a single industrial-scale HPMS batch (Section 2.1), which avoided feedstock variability between conditions but limited the amount of material and, with it, the number of complementary analyses. The absolute position of the window may shift for feedstocks with different composition, oxygen content, or particle size; for this reason, it is reported as a phenomenological window for this class of EoL wind-turbine magnets.

4. Conclusions

In conclusion, this study establishes a phenomenological degassing window for the recovery of the magnetic properties of recycled NdFeB powders derived from EoL wind-turbine magnets through a simple "magnet-to-magnet" process that involves hydrogen processing, jet milling, and controlled vacuum degassing. Degassing temperature was varied systematically at a fixed heating rate, and heating rate was screened at 900 °C, in relation to hydrogen desorption behavior and magnetic properties. Under the investigated conditions, a heating rate of 2 °C/min and annealing temperatures around 840–900 °C provided the most favorable overall balance between coercivity and M(1700 kA m^{-1}). The highest coercivity was obtained after degassing at 900 °C (434.1 kA/m), while the highest M(1700 kA m^{-1}) was achieved at 880 °C (99.8 A·m^2/kg). These results highlight the

importance of controlling the thermal history of HPMS-derived powders to tailor their magnetic response.

Deconvolution of the hydrogen desorption traces resolved three components, attributed on the basis of the literature to hydrogen release from $Nd_2Fe_{14}BH_x$, the $NdH_{2.7} \rightarrow NdH_2$ transition, and the decomposition of NdH_2. First-order (Redhead) estimates of the corresponding activation energies (~111–127, 131–150, and 214–245 kJ mol^{-1}) depend on the assumed kinetic order and pre-exponential factor, but their ordering identifies NdH_2 decomposition as the most demanding step, consistent with the lower bound of the degassing window. The coercivity recovery above 840 °C is tentatively attributed to the recombination of α-Fe and Nd into $Nd_2Fe_{14}B$, which remains to be confirmed.

Three findings stand out: (i) The thermal history affects the magnetic properties of the degassed powder, with 2 °C/min giving the best balance among the conditions tested. Heating rate and time at temperature were not fully decoupled, but at comparable time above 800 °C coercivity depends primarily on the peak degassing temperature. (ii) For powder from EoL wind-turbine magnets, degassing at ~900 °C maximizes coercivity and at ~880 °C maximizes M(1700 kA m^{-1}). (iii) Because no sintering step follows when the powder is used in polymer-bonded magnets, HPMS jet-milled powder requires a degassing window different from the ~600–700 °C protocols established for re-sintering [41,44]. The oxygen content (0.66 ± 0.06 wt.% after degassing) and the coercivity (≤434 kA/m) remain below the requirements of high-performance bonded magnets.

Follow-up work should (1) identify the phases before and after degassing by XRD and Mössbauer spectroscopy to quantify the formation and consumption of α-Fe, (2) screen dwell time at a fixed heating rate, and heating rate at a fixed total time at temperature, in the 840–900 °C range, (3) measure the oxygen and hydrogen contents (inert-gas fusion) and the specific surface area (BET) for every condition and correlate them with coercivity and with the integrated desorption signal, and (4) fabricate and characterize bonded magnets (density, microstructure, H_{cj}, B_r, and $(BH)_{max}$) to establish whether the properties of the powder translate into the final component.

Author Contributions: Conceptualization, A.B., J.F.F. and A.Q.; methodology, A.B., B.P., S.K., C.B., J.F.F. and A.Q.; software, A.B. and A.Q.; validation, B.P., S.K., J.F.F. and A.Q.; formal analysis, A.B., B.P. and A.Q.; investigation, A.B., B.P. and A.Q.; resources, B.P., S.K., L.G., C.B., J.F.F. and A.Q.; data curation, A.B. and A.Q.; writing—original draft preparation, A.B. and A.Q.; writing—review and editing, A.B., L.G., J.F.F. and A.Q.; visualization, A.B.; supervision, B.P., S.K. and A.Q.; project administration, A.Q.; funding acquisition, A.Q. All authors have read and agreed to the published version of the manuscript.

Funding: This work has been supported by the JECS Trust, Fund Contract No. 2022319, the INSPIRES project funded by the EIT RawMaterials under grant number 20090, the BEETHOVEN project funded by the European Commission under grant agreement 101129912, and the GENIUS project funded by the Ministerio de Ciencia, Innovación y Universidades/Agencia Estatal de Investigación (MCIN/AEI/10.13039/501100011033) through Grant PCI2024-153493. Also, this work has been supported by grants TED2021-130957B-C51 and CNS2022-135876 funded by MICIU/AEI/10.13039/501100011033. Views and opinions expressed are, however, those of the authors only and do not necessarily reflect those of the European Union or the European Education and Culture Executive Agency (EACEA). Neither the European Union nor EACEA can be held responsible for them.

Data Availability Statement: The original contributions presented in this study are included in the article. Further inquiries can be directed to the corresponding authors.

Conflicts of Interest: The authors declare no conflicts of interest.

Abbreviations

The following abbreviations are used in this manuscript:

Abbreviation	Definition
BSE	Backscattered electron
CRM	Critical raw material
DSC	Differential scanning calorimetry
EDS	Energy-dispersive X-ray spectroscopy
EoL	End-of-life
FD	Full degassing
FEGSEM	Field-emission-gun scanning electron microscopy
GBP	Grain boundary phase
HD	Hydrogen decrepitation/hydrogen-decrepitated
HDD	Hard disk drive
HDDR	Hydrogenation–disproportionation–desorption–recombination
HPMS	Hydrogen processing of magnetic scrap
HRE	Heavy rare earth
ICP-MS	Inductively coupled plasma mass spectrometry
ICP-OES	Inductively coupled plasma optical emission spectrometry
JM	Jet milling/jet-milled
LRE	Light rare earth
NdFeB	Neodymium–iron–boron
PD	Partial degassing
PEM	Powder extrusion molding
P–T	Pressure–temperature
REE	Rare-earth element
RT	Room temperature
SEM	Scanning electron microscopy
TGA	Thermogravimetric analysis
VCM	Voice-coil motor
VSM	Vibrating sample magnetometer
XRD	X-ray diffraction

References

1. Sugimoto, S. Current status and recent topics of rare-earth permanent magnets. *J. Phys. D. Appl. Phys.* **2011**, *44*, 064001. [CrossRef]
2. Brown, D.; Ma, B.-M.; Chen, Z. Developments in the processing and properties of NdFeB-type permanent magnets. *J. Magn. Magn. Mater.* **2002**, *248*, 432–440. [CrossRef]
3. Yang, Y.; Walton, A.; Sheridan, R.; Güth, K.; Gauß, R.; Gutfleisch, O.; Buchert, M.; Steenari, B.-M.; Van Gerven, T.; Jones, P.T.; et al. REE recovery from end-of-life NdFeB permanent magnet scrap: A critical review. *J. Sustain. Metall.* **2017**, *3*, 122–149. [CrossRef]
4. Deng, C.; Zhang, X.; Guo, F.; Wang, S.; Wang, X. The current status of recycling technology for waste NdFeB resources. *J. Mater. Cycles Waste Manag.* **2025**, *27*, 796–811. [CrossRef]
5. Rizos, V.; Righetti, E.; Kassab, A. *Developing a Supply Chain for Recycled Rare Earth Permanent Magnets in the EU: Challenges and Opportunities*; CEPS: Brussels, Belgium, 2022.
6. Firdaus, M.; Rhamdhani, M.A.; Durandet, Y.; Rankin, W.J.; McGregor, K. Review of high-temperature recovery of rare earth (Nd/Dy) from magnet waste. *J. Sustain. Metall.* **2016**, *2*, 276–295. [CrossRef]
7. Bian, Y.Y.; Guo, S.Q.; Xu, Y.L.; Tang, K.; Lu, X.G.; Ding, W.Z. Recovery of rare earth elements from permanent magnet scraps by pyrometallurgical process. *Rare Met.* **2022**, *41*, 1697–1702. [CrossRef]
8. Rasheed, M.Z.; Nam, S.W.; Cho, J.Y.; Park, K.T.; Kim, B.S.; Kim, T.S. Review of the liquid metal extraction process for the recovery of Nd and Dy from permanent magnets. *Metall. Mater. Trans. B* **2021**, *52*, 1213–1227. [CrossRef]
9. Behera, S.S.; Parhi, P.K. Leaching kinetics study of neodymium from the scrap magnet using acetic acid. *Sep. Purif. Technol.* **2016**, *160*, 59–66. [CrossRef]
10. Rabatho, J.P.; Tongamp, W.; Takasaki, Y.; Haga, K.; Shibayama, A. Recovery of Nd and Dy from rare earth magnetic waste sludge by hydrometallurgical process. *J. Mater. Cycles Waste Manag.* **2013**, *15*, 171–178. [CrossRef]
11. Zhang, Y.; Gu, F.; Su, Z.; Liu, S.; Anderson, C.; Jiang, T. Hydrometallurgical recovery of rare earth elements from NdFeB permanent magnet scrap: A review. *Metals* **2020**, *10*, 841. [CrossRef]
12. Lewis, L.H.; Jiménez-Villacorta, F. Perspectives on permanent magnetic materials for energy conversion and power generation. *Metall. Mater. Trans. A* **2013**, *44*, 2–20. [CrossRef]

13. Binnemans, K.; Jones, P.T.; Blanpain, B.; Van Gerven, T.; Yang, Y.; Walton, A.; Buchert, M. Recycling of rare earths: A critical review. *J. Clean. Prod.* **2013**, *51*, 1–22. [CrossRef]
14. Zakotnik, M.; Tudor, C.O.; Peiró, L.T.; Afiuny, P.; Skomski, R.; Hatch, G.P. Analysis of energy usage in Nd–Fe–B magnet to magnet recycling. *Environ. Technol. Innov.* **2016**, *5*, 117–126. [CrossRef]
15. Walton, A.; Williams, A. Rare earth recovery. *Mater. World* **2011**, *19*, 24–26.
16. Burkhardt, C.; van Nielen, S.; Awais, M.; Bartolozzi, F.; Blomgren, J.; Ortiz, P.; Xicotencatl, M.; Degri, M.; Nayebossadri, S.; Walton, A. An overview of hydrogen assisted (direct) recycling of rare earth permanent magnets. *J. Magn. Magn. Mater.* **2023**, *588*, 171475. [CrossRef]
17. Chen, Z.; Miller, D.; Herchenroeder, J. High performance nanostructured Nd–Fe–B fine powder prepared by melt spinning and jet milling. *J. Appl. Phys.* **2010**, *107*, 09A730. [CrossRef]
18. McGuiness, P.J.; Devlin, E.; Harris, I.R.; Rozendaal, E.; Ormerod, J. A study of NdFeB magnets produced using a combination of hydrogen decrepitation and jet milling. *J. Mater. Sci.* **1989**, *24*, 2541–2548. [CrossRef]
19. Hono, K.; Sepehri-Amin, H. Strategy for high-coercivity Nd–Fe–B magnets. *Scr. Mater.* **2012**, *67*, 530–535. [CrossRef]
20. Soderžnik, K.Ž.; Rožman, K.Ž.; Komelj, M.; Kovács, A.; Diehle, P.; Denneulin, T.; Savenko, A.; Soderžnik, M.; Kobe, S.; Dunin-Borkowski, R.E.; et al. Microstructural insights into the coercivity enhancement of grain-boundary-diffusion-processed Tb-treated NdFeB sintered magnets beyond the core-shell formation mechanism. *J. Alloys Compd.* **2021**, *864*, 158915. [CrossRef]
21. Li, W.F.; Ohkubo, T.; Hono, K.; Sagawa, M. The origin of coercivity decrease in fine grained Nd–Fe–B sintered magnets. *J. Magn. Magn. Mater.* **2009**, *321*, 1100–1105. [CrossRef]
22. Vasilenko, D.Y.; Shitov, A.V.; Bratushev, D.Y.; Podkorytov, K.I.; Gaviko, V.S.; Golovnya, O.A.; Popov, A.G. Magnetic hysteresis properties and microstructure of high-energy (Nd,Dy)–Fe–B magnets with low oxygen content. *Phys. Met. Metallogr.* **2021**, *122*, 1173–1182. [CrossRef]
23. Li, W.F.; Ohkubo, T.; Hono, K.; Nishiuchi, T.; Hirosawa, S. The role of grain boundaries in the coercivity of hydrogenation disproportionation desorption recombination processed Nd–Fe–B powders. *J. Appl. Phys.* **2009**, *105*, 07A706. [CrossRef]
24. Saje, B.; Holc, J.; Beseničar, S. The sequence of fracture processes in hydrogen-decrepitated $Nd_{16-x}Dy_xFe_{76}B_8$ alloy. *J. Magn. Magn. Mater.* **1991**, *101*, 357–359. [CrossRef]
25. Nan, H.; Zhu, L.; Liu, H.; Li, W. Effect of cathodic hydrogen evolution on the coercivity and thermal stability of sintered NdFeB magnets. *Rare Met. Mater. Eng.* **2017**, *46*, 3658–3662. [CrossRef]
26. Oesterreicher, K.; Oesterreicher, H. Structure and magnetic properties of $Nd_2Fe_{14}BH_{2.7}$. *Phys. Status Solidi A* **1984**, *85*, K61–K64. [CrossRef]
27. Wiesinger, G.; Hilscher, G.; Grössinger, R. Effect of hydrogen absorption on the magnetic properties of $Nd_{15}Fe_{77}B_8$. *J. Less-Common Met.* **1987**, *131*, 409–417. [CrossRef]
28. Fruchart, D.; Miraglia, S.; De Rango, P.; Wolfers, P. Hydrogen location in hard magnet materials: Scheme, fundamental aspects, processes. *J. Alloys Compd.* **2004**, *383*, 17–22. [CrossRef]
29. Zakotnik, M.; Devlin, E.; Harris, I.R.; Williams, A.J. Hydrogen decrepitation and recycling of NdFeB-type sintered magnets. *J. Iron Steel Res. Int.* **2006**, *13*, 289–295. [CrossRef]
30. Sheridan, R.S.; Williams, A.J.; Harris, I.R.; Walton, A. Improved HDDR processing route for production of anisotropic powder from sintered NdFeB type magnets. *J. Magn. Magn. Mater.* **2014**, *350*, 114–118. [CrossRef]
31. Li, X.; Yue, M.; Zakotnik, M.; Liu, W.; Zhang, D.; Zuo, T. Regeneration of waste sintered NdFeB magnets to fabricate anisotropic bonded magnets. *J. Rare Earths* **2015**, *33*, 736–739. [CrossRef]
32. Habibzadeh, A.; Kucuker, M.A.; Çakır, Ö.; Gökelma, M. Microstructural investigation of discarded NdFeB magnets after low-temperature hydrogenation. *J. Sustain. Metall.* **2024**, *10*, 1141–1155. [CrossRef]
33. Nayebossadri, S.; Awais, M.; Arnold, R.; Degri, M.; Mann, N.; Walton, A. Hydrogen-assisted recycling of NdFeB magnets from the end-of-life audio products. *J. Magn. Magn. Mater.* **2024**, *603*, 172239. [CrossRef]
34. Mishra, A.; Khoshsima, S.; Tomše, T.; Podmiljšak, B.; Šturm, S.; Burkhardt, C.; Žužek, K. Short-loop recycling of NdFeB permanent magnets: A sustainable solution for the $RE_2Fe_{14}B$ matrix phase recovery. *Materials* **2023**, *16*, 6565. [CrossRef] [PubMed]
35. Gutfleisch, O.; Harris, I.R. Fundamental and practical aspects of the hydrogenation, disproportionation, desorption and recombination process. *J. Phys. D Appl. Phys.* **1996**, *29*, 2255. [CrossRef]
36. Gutfleisch, O.; Güth, K.; Woodcock, T.G.; Schultz, L. Recycling used NdFeB sintered magnets via a hydrogen-based route to produce anisotropic, resin bonded magnets. *Adv. Energy Mater.* **2013**, *3*, 151–155. [CrossRef]
37. Li, C.; Yue, M.; Liu, W.; Zuo, T.; Yi, X.; Chen, J.; Zhou, Z.; Wu, Y. Recycling of scrap sintered Nd–Fe–B magnets as anisotropic bonded magnets via hydrogen decrepitation process. *J. Mater. Cycles Waste Manag.* **2015**, *17*, 547–552. [CrossRef]
38. Hauck, P.A. Powder injection molding: Current and long term outlook. *Int. J. Powder Metall.* **2000**, *36*, 29–30.
39. Grönefeld, M. Review on bonded magnets. In *Bonded Magnets*; Hadjipanayis, G.C., Ed.; NATO Science Series II; Springer: Dordrecht, The Netherlands, 2003; Volume 118, pp. 1–12. [CrossRef]

40. Hadjipanayis, G.C. (Ed.) *Bonded Magnets: Proceedings of the NATO Advanced Research Workshop on Science and Technology of Bonded Magnets, Newark, DE, USA*; Springer: Dordrecht, The Netherlands, 2003.
41. Zakotnik, M.; Harris, I.R.; Williams, A.J. Possible methods of recycling NdFeB-type sintered magnets using the HD/degassing process. *J. Alloys Compd.* **2008**, *450*, 525–531. [CrossRef]
42. Önal, M.A.R.; Jönsson, C.; Zhou, W.; Van Gerven, T.; Guo, M.; Walton, A.; Blanpain, B. Comparative oxidation behavior of NdFeB magnets for potential recycling methods: Effect of hydrogenation pre-treatment and magnet composition. *J. Alloys Compd.* **2017**, *728*, 727–738. [CrossRef]
43. Rathfelder, S.; Schuschnigg, S.; Kukla, C.; Holzer, C.; Suess, D.; Burkhardt, C. Process optimization to produce anisotropic NdFeB permanent magnets from recycled powder via powder extrusion. *Sci. Rep.* **2025**, *15*, 35284. [CrossRef] [PubMed]
44. Williams, A.J.; McGuiness, P.J.; Harris, I.R. Mass spectrometer hydrogen desorption studies on some hydrided NdFeB-type alloys. *J. Less-Common Met.* **1991**, *171*, 149–155. [CrossRef]
45. Kozak, V.; Pickering, L.; Awais, M.; Mahendran, A.; Farthing, J.G.; Arnold, R.; Mann, N.; Brown, D.; Walton, A. Improving short-loop recycling of sintered NdFeB magnets by grain boundary phase separation following hydrogen processing. *Sustain. Mater. Technol.* **2025**, *46*, e01744. [CrossRef]
46. Redhead, P.A. Thermal desorption of gases. *Vacuum* **1962**, *12*, 203–211. [CrossRef]
47. Schneider, C.A.; Rasband, W.S.; Eliceiri, K.W. NIH Image to ImageJ: 25 years of image analysis. *Nat. Methods* **2012**, *9*, 671–675. [CrossRef] [PubMed]
48. Yan, G.; McGuiness, P.J.; Farr, J.P.G.; Harris, I.R. Optimisation of the processing of Nd–Fe–B with dysprosium addition. *J. Alloys Compd.* **2010**, *491*, L20–L24. [CrossRef]
49. Oono, N.; Sagawa, M.; Kasada, R.; Matsui, H.; Kimura, A. Production of thick high-performance sintered neodymium magnets by grain boundary diffusion treatment with dysprosium–nickel–aluminum alloy. *J. Magn. Magn. Mater.* **2011**, *323*, 297–300. [CrossRef]
50. Nishino, M.; Hayasaka, H.; Miyashita, S. Thermodynamic properties of $R_2Fe_{14}B$ (R = Dy, Nd) and dysprosium random substitution effect on coercivity in neodymium permanent magnets. *J. Appl. Phys.* **2024**, *136*, 033904. [CrossRef]
51. Banda, R.; Jeon, H.S.; Lee, M.S. Separation of Nd from mixed chloride solutions with Pr by extraction with saponified PC 88A and scrubbing. *J. Ind. Eng. Chem.* **2015**, *21*, 436–442. [CrossRef]
52. Zeng, H.; Liu, Z.; Li, W.; Zhang, J.; Zhao, L.; Zhong, X.; Yu, H.; Guo, B. Significantly enhancing the coercivity of NdFeB magnets by ternary Pr-Al-Cu alloys diffusion and understanding the elements diffusion behavior. *J. Magn. Magn. Mater.* **2019**, *471*, 97–104. [CrossRef]
53. Khoshsima, S.; Vidmar, J.; Samardžija, Z.; Tomše, T.; Kušter, M.; Mishra, A.; Šturm, S.; Žužek, K. Environmentally friendly approach for $Nd_2Fe_{14}B$ magnetic phase extraction by selective chemical leaching: A proof-of-concept study. *Materials* **2023**, *16*, 5181. [CrossRef] [PubMed]
54. Isotahdon, E.; Huttunen-Saarivirta, E.; Kuokkala, V.T. Characterization of the microstructure and corrosion performance of Ce-alloyed NdFeB magnets. *J. Alloys Compd.* **2017**, *692*, 190–197. [CrossRef]
55. Hirosawa, S.; Kanekiyo, H. Nanostructure and magnetic properties of chromium-doped Fe_3B-$Nd_2Fe_{14}B$ exchange-coupled permanent magnets. *Mater. Sci. Eng. A* **1996**, *217–218*, 367–370. [CrossRef]
56. Zhong, S.; Yang, M.; Wang, H.; Rehman, S.U.; Yu, X.; Luo, S.; Li, L.; Li, C.; Xiong, S.; Yang, B. Grain boundary diffusion efficiency of sintered NdFeB magnets by Al, Sn and Zn addition. *J. Alloys Compd.* **2023**, *967*, 171676. [CrossRef]
57. Nothnagel, P.; Müller, K.-H.; Eckert, D.; Handstein, A. The influence of particle size on the coercivity of sintered NdFeB magnets. *J. Magn. Magn. Mater.* **1991**, *101*, 379–381. [CrossRef]
58. Book, D.; Harris, I.R. Hydrogen absorption/desorption and HDDR studies on $Nd_{16}Fe_{76}B_8$ and $Nd_{11\cdot8}Fe_{82\cdot3}B_{5\cdot9}$. *J. Alloys Compd.* **1995**, *221*, 187–192. [CrossRef]
59. Rupp, B.; Resnik, A.; Shaltiel, D.; Rogl, P. Phase relations and hydrogen absorption of neodymium-iron-(boron) alloys. *J. Mater. Sci.* **1988**, *23*, 2133–2141. [CrossRef]
60. Habibzadeh, A.; Kucuker, M.A.; Gökelma, M. Review on the parameters of recycling NdFeB magnets via a hydrogenation process. *ACS Omega* **2023**, *8*, 17431–17445. [CrossRef] [PubMed]
61. Williams, A.J.; McGuiness, P.J.; Harris, I.R. Mass spectrometer studies of hydrogen desorption from hydrided NdFeB. *IEEE Trans. Magn.* **1990**, *26*, 1945–1947. [CrossRef]
62. Kissinger, H.E. Reaction kinetics in differential thermal analysis. *Anal. Chem.* **1957**, *29*, 1702–1706. [CrossRef]
63. Bai, G.; Gao, R.W.; Sun, Y.; Han, G.B.; Wang, B. Study of high-coercivity sintered NdFeB magnets. *J. Magn. Magn. Mater.* **2007**, *308*, 20–23. [CrossRef]
64. Berja, A.; Granados-Miralles, C.; Serrano, A.; López-Sánchez, J.; Marco, J.F.; Grau, L.; Burkhardt, C.; Fernández, J.F.; Quesada, A. Insights into the structural, chemical and magnetic evolution of HPMS NdFeB powders milled in air. *J. Alloys Compd.* **2026**, *1082*, 191635. [CrossRef]

65. Burkhardt, C.; Weber, O.; Podmiljsak, B.; Gonzalez-Gutierrez, J.; Kukla, C.; Degri, M.; Harris, I.R.; Walton, A. Isotropic NdFeB hard magnets: MIM production using recycled powders with and without Nd additions. *Powder Inject. Mould. Int.* **2017**, *11*, 75–81.
66. Choi, Y.; Jiang, J.S.; Ding, Y.; Rosenberg, R.A.; Pearson, J.E.; Bader, S.D.; Zambano, A.; Murakami, M.; Takeuchi, I.; Wang, Z.L.; et al. Role of diffused Co atoms in improving effective exchange coupling in Sm-Co/Fe spring magnets. *Phys. Rev. B* **2007**, *75*, 104432. [CrossRef]
67. Guzmán-Mínguez, J.C.; Granados-Miralles, C.; Kuntschke, P.; Fernández, C.d.J.; Erokhin, S.; Berkov, D.; Schliesch, T.; Fernández, J.F.; Quesada, A. Remanence increase in $SrFe_{12}O_{19}$/Fe exchange-decoupled hard-soft composite magnets owing to dipolar interactions. *Nanomaterials* **2023**, *13*, 2097. [CrossRef] [PubMed]
68. Quesada, A.; Granados-Miralles, C.; López-Ortega, A.; Erokhin, S.; Lottini, E.; Pedrosa, J.; Bollero, A.; Aragón, A.M.; Rubio-Marcos, F.; Stingaciu, M.; et al. Energy product enhancement in imperfectly exchange-coupled nanocomposite magnets. *Adv. Electron. Mater.* **2016**, *2*, 1500365. [CrossRef]
69. Ma, B.-M.; Herchenroeder, J.W.; Smith, B.; Suda, M.; Brown, D.N.; Chen, Z. Recent development in bonded NdFeB magnets. *J. Magn. Magn. Mater.* **2002**, *239*, 418–423. [CrossRef]
70. Zakotnik, M.; Harris, I.R.; Williams, A.J. Multiple recycling of NdFeB-type sintered magnets. *J. Alloys Compd.* **2009**, *469*, 314–321. [CrossRef]

Disclaimer/Publisher's Note: The statements, opinions and data contained in all publications are solely those of the individual author(s) and contributor(s) and not of MDPI and/or the editor(s). MDPI and/or the editor(s) disclaim responsibility for any injury to people or property resulting from any ideas, methods, instructions or products referred to in the content.